Advanced Imaging of Head and Neck Infections

Short running title: Advanced Imaging of Head and Neck Infections

Akira Baba[1]*, Ryo Kurokawa[1], Mariko Kurokawa[1], Scott Reifeiss[2], Bruno A. Policeni[2], Yoshiaki Ota[1], Ashok Srinivasan[1]

Akira Baba, MD, PhD:

1. *Division of Neuroradiology, Department of Radiology, University of Michigan*
2. *Department of Radiology, Roy Caver College of Medicine, The University of Iowa*

Correspondence:

Akira Baba, MD, PhD

E-mail: akirababa0120@gmail.com

Division of Neuroradiology, Department of Radiology, University of Michigan, 1500 E. Medical Center Dr., Ann Arbor, MI, 48109, USA

Phone number: +1-734-882-5298

Keywords

head and neck infection; magnetic resonance imaging; apparent diffusion coefficient; metal artefact reduction; dual-energy CT; subtraction CT technique

Funding

None.

Abstract

When head and neck infection is suspected, appropriate imaging contributes to treatment decisions and prognosis. While contrast-enhanced CT is the standard imaging modality for evaluating head and neck infections, MRI can better characterize the skull base, intracranial involvement, and osteomyelitis, implying that these are complementary techniques for a comprehensive assessment. Both CT and MRI are useful in the evaluation of abscesses and thrombophlebitis, while MRI is especially useful in the evaluation of intracranial inflammatory spread/abscess formation, differentiation of abscess from other conditions, evaluation of the presence and activity of inflammation and osteomyelitis, evaluation of mastoid extension in middle ear cholesteatoma, and evaluation of facial neuritis and labyrinthitis. Apparent diffusion coefficient derived from diffusion-weighted imaging is useful for differential diagnosis of and treatment response of head and neck infections in various anatomical sites. Dynamic contrast-enhanced MRI perfusion may be useful in

assessing the activity of skull base osteomyelitis. MR bone imaging may be of additional value in evaluating bony structures of the skull base and jaw. Dual energy CT is helpful in reducing metal artifacts, evaluating deep neck abscess, and detecting salivary stones. Subtraction CT techniques are used to detect progressive bone-destructive changes and to reduce dental amalgam artifacts. This article provides a region-based approach to the imaging evaluation of head and neck infections, using both conventional and advanced imaging techniques.

INTRODUCTION

Head and neck infections require rapid diagnosis and intervention due to their proximity to critical neurovascular structures including the brain and spinal cord. Radiological imaging plays a critical role in depicting the location and extent of the disease, identifying the origin of infection, and detecting associated complications. Delayed clinical intervention increases the risk of complications and the spread of infection, which can compromise critical anatomical structures such as the airway, blood vessels, optic nerves, and intracranial structures.

Contrast-enhanced CT is the first and standard imaging modality of choice in head and neck infections. Its advantages include immediate availability, cost-effectiveness, short

examination time with rapid data acquisition, and thus minimal motion artifacts which are potentially caused by swallowing and eye movements. Contrast-enhanced CT is also well suited for identifying the origin of infection and its extension into the deep neck spaces.[1] CT with a bone reconstruction kernel is an excellent imaging modality for the temporal bone and paranasal sinuses. Although CT has many of these advantages, metal artifacts associated with dental treatment can degrade image quality and obscure the depiction of infectious diseases of the oral cavity or oropharynx.[2] Various state-of-the-art techniques including virtual monochromatic imaging derived from dual-energy CT, subtraction CT technique and artifact reduction algorithm described later in this article, can be useful to mitigate these artifacts. In addition, dual energy CT can produce non-contrast CT-like virtual unenhanced images that are useful for the detection of sialoliths.[3] MRI is not used as the first or only imaging modality in emergency situations due to some disadvantages such as limited availability, relatively long scan times, and patient access related to implantable devices and claustrophobia. However, MRI has unique advantages compared to CT, including higher contrast resolution, detection sensitivity for detecting head and neck abscesses,[4,5] and a tendency for less image quality degradation due to metal artifacts associated with dental treatment.[6] Additionally, MRI is superior in evaluating intracranial spread of head and neck infections and assessment of abnormal bone marrow intramedullary signal intensity in the

skull base and maxillofacial bone.[1] Despite the limited research on advanced imaging in head and neck infections, some studies have focused on the widely used techniques of diffusion-weighted imaging (DWI) and apparent diffusion coefficient (ADC). These techniques are recognized for their clinical relevance and applicability. In addition, recent developments that can reduce artifacts, such as zoomed DWI reported in the abdominal region,[7] may further improve image quality in the head and neck region. ^{18}F-fludeoxyglucose (FDG) PET/CT has been employed to assess head and neck malignancies and whole body systemic infections and inflammation,[8,9] while its use in head and neck infections is confined to the skull base and dental areas.[10,11] To date, the role of newer imaging techniques in head and neck infections has not been adequately described. Knowledge of advanced imaging is necessary to avoid unnecessary additional examinations. In this article, we present a region-based approach to contemporary imaging evaluation of head and neck infections.

A. Orbital/sinonasal region

Orbital complications associated with paranasal sinus infectious disease

Due to their close anatomical relationship, orbital infections are often associated with rhinosinusitis.[12,13] On MRI, fat-suppressed sequences such as short tau inversion recovery (STIR) and fat-suppressed T2-weighted image (T2WI) are useful for detecting and

assessing the extent of the orbital cellulitis (Fig. 1A).[14,15] DWI adds diagnostic reliability in detecting suborbital periosteal abscesses by characteristically showing diffusion restriction within the orbital structures (Fig. 1D, E),[16,17] which is particularly useful in patients in whom contrast is contraindicated.[18] MRI is recommended in cases of clinical suspicion of superior ophthalmic vein or cavernous sinus thrombosis,, intracranial abscesses, or meningitis that may be associated with orbital infections.[17] Orbital thrombophlebitis shows high signal intensity within an enlarged vein on nonenhanced T1-weighted image (T1WI) or as an enhancement defect in a dilated vein on post-contrast T1WI,[18,19] with the thrombus showing high signal on DWI.[20]

Intracranial complications associated with paranasal sinus infection

Paranasal sinus infection could be associated with complications such as meningitis, epidural abscess, subdural abscess, intracerebral abscess, encephalitis, and venous sinus thrombosis,[13,21] although these are less common than those in the orbit.[22] Post-contrast MRI is superior to Contrast-enhanced CT in evaluating intracranial complications associated with sinusitis.[23] Classic imaging features of meningeal involvement on MRI include abnormal leptomeningeal enhancement adjacent to the sinuses on post-contrast T1WI (Fig. 2A)[12] and high signal extending into a sulcus on fluid attenuated inversion recovery (FLAIR) images (as a result of high protein concentration of cerebrospinal fluid due to leptomeningeal

inflammation).[24] Post-contrast FLAIR imaging is also used to diagnose meningitis.[25] Most commonly, spread of infection from the paranasal sinuses to the intracranial compartment causes subdural and epidural abscesses[15] seen as fluid signal intensity lesions with a rim-like enhancement effect between the skull and cerebral parenchyma (Fig. 2A), and additionally demonstrating diffusion restriction on DWI (Fig. 2B, C).[15] The "double rim sign (surrounded by two concentric rims, with the outer rim showing low signal intensity and the inner rim showing high signal intensity)" on susceptibility weighted imaging is considered a characteristic finding of intracranial pyogenic abscess[26] and may be useful in the diagnosis of this entity (Fig. 3).

Noninvasive Fungal Rhinosinusitis

Noninvasive fungal rhinosinusitis includes pathologies such as allergic fungal rhinosinusitis (AFRS) and fungal ball formation.[27] AFRS is seen as unilateral or bilateral mucosal thickening and allergic mucin characterized by markedly low signal intensity on T2WI (Fig. 4A).[27,28] AFRS and eosinophilic mucin rhinosinusitis both have similar CT findings of characteristic eosinophilic allergic mucin with a high density component; however, AFRS has been reported to have lower signal intensity on T2WI than eosinophilic mucin rhinosinusitis.[29] ADC values derived from DWI have been reported to be significantly lower in fungal sinusitis (mean ADC value, 0.98×10^{-3} mm^2/s) than in other inflammatory

lesions (Fig. 4B).[30] Fungal ball formation is suspected when MRI shows markedly low signal intensity on T2WI.[12,31] Recently, it has been reported that high-signal intensity findings on T1WI are also characteristic of fungal ball formation (Fig. 5).[32]

Invasive fungal rhinosinusitis

Invasive fungal rhinosinusitis is classified into acute or chronic invasive and chronic granulomatous forms[33] and is characterized by thickening of the soft tissues of the nasal cavity (especially the middle turbinate), ethmoid and sphenoid sinuses, and as bone destruction progresses, extension into fat pad, pterygopalatine fossa,intracranial region, cavernous sinus, and orbit.[33,34] MRI is useful in the diagnosis and evaluation of orbital and intracranial spread.[33] Intracranial involvement of invasive fungal sinusitis may present as reactive edema, leptomeningeal enhancement, granulomas and abscesses on MRI.[33,34] Invasive fungal paranasal sinusitis causes tissue ischemia, therefore contrast-enhanced T1WI shows lack of contrast enhancement in normally enhancing structures such as the mucosal surfaces of the nasal cavities and turbinates ("black turbinate sign")(Fig. 6 A, B).[35] Chronic invasive fungal sinusitis has been reported to show characteristic MRI features of heterogeneous low signal on T2WI with lack of contrast enhancement on post-contrast T1WI, distinguishing it from sinonasal tumors (Fig. 6).[36] There are reports suggesting that a pattern

of lack of contrast enhancement on MRI was the only independent prognostic factor for disease-specific mortality in acute invasive fungal sinusitis.[37]

B. Temporal bone/skull base

Necrotizing otitis externa and skull base osteomyelitis

Necrotizing otitis externa is common in elderly diabetic or immunocompromised patients, and is caused by an infection of the external auditory canal caused by *Pseudomonas aeruginosa*, which can progress to skull base osteomyelitis via the temporal bone.[38] MRI is highly sensitive for detecting changes in the skull base bone marrow, and provides the most comprehensive and accurate assessment for monitoring response to treatment, and assessing intracranial extension compared to CT.[1,38,39] MRI findings include variable low to high signal intensity on T2WI, low signal intensity on T1WI, and diffuse enhancement on post-contrast fat-suppressed T1WI (Fig. 7A, 8A).[40,41] Additionally, MR venography and MR angiography are useful when venous thrombosis or carotid artery occlusion is suspected.[40] Skull base osteomyelitis tends to have higher ADC values derived from DWI compared to malignancy (mean ADC values of osteomyelitis of the skull base, $1.26 \times 10^{-3}mm^2$; malignancy, 0.59–0.99 $\times 10^{-3}mm^2$), which may be helpful in the differentiation (Fig. 7B).[42,43] The advanced MRI technique, MR bone imaging[44,45] may be of additional value in visualizing skull base

destruction (Fig. 9). Bone subtraction iodine CT imaging has been reported to be useful in evaluating skull base invasion by nasopharyngeal carcinoma,[46] and this subtraction CT technique may also be useful in evaluating the activity of skull base osteomyelitis. The optimal imaging modality for evaluating treatment response in skull base osteomyelitis is controversial due to the scarcity of reported data;[39] however, MRI and CT are often commonly used to determine treatment response. Since imaging findings associated with skull base infection may persist for some period after treatment, this makes an accurate assessment difficult.[39,47] Reduction of high signal intensities on the ADC map has been reported to reflect the treatment response (Fig. 7 B, C).[48] Temporal subtraction CT technique, subtracting images of a previous CT from a current CT that is reported to be useful in detecting middle ear cholesteatoma and recurrent progressive bone erosion,[49,50,51] may have utility in evaluating the treatment response if follow-up CTs are performed. Because of its wide clinical availability, superior spatial resolution, and reduced radiation exposure compared with gallium scintigraphy, ^{18}F-FDG-PET/CT should be considered as one of the additional imaging modalities for the initial diagnosis and follow-up of necrotizing otitis externa and skull base osteomyelitis (Fig. 8B).[39,10] In the future, new imaging modalities such as PET-MRI with advantages such as superior soft tissue detail evaluation, reduced radiation exposure, and shorter imaging time compared to PET-CT may play a greater role in the

follow-up.[40] One of the dynamic contrast-enhanced MRI parameters, Ve (fraction of the extravascular extracellular space) was moderately high (median, 0.48)[43] in the pretreatment status (Fig. 8C), and its quantitative decrease after treatment may reflect a treatment response.

Coalescent mastoiditis

Acute mastoiditis is the most common complication of acute otitis media, and acute coalescent mastoiditis occurs when a mucoperiosteal infection in a mastoid cell spreads to the bones.[52] The most common complications seen on MRI are intratemporal abscess (23%), subperiosteal abscess (19%), and labyrinthine involvement (16%).[53] These abscesses are associated with rim enhancement on contrast-enhanced T1WI (Fig. 10A) and high signal intensity of the contents on DWI.[52,53,54] ADC values greater than 1.2×10^{-3} mm^2/s have been reported to have a negative predictive value of 92% for complicated coalescent mastoiditis[55] (Fig. 10). Lesions with erosion of the medial wall/sigmoid sinus plate cause thrombosis involving the adjacent sigmoid sinus,[1,54] which can be identified as loss of signal voids on spin-echo MR sequences(Fig. 11A), intravenous contrast defects on post-contrast T1WI (Fig.11B), lack of flow-related enhancement on MR venography/gradient-echo sequences (Fig. 11C), and high signal on DWI.[12,18]

Petrous apicitis

Petrous apicitis is typically caused by medial spread of infection to the pneumatized petrous apex from acute otorhinolaryngitis.[1] MRI may show high signal intensity on STIR/fat-suppressed T2WI (Fig. 12A) and enhancement on post-contrast T1WI, usually in the early stages, or additional enhancement of the adjacent dura in the advanced stage.[1,56] DWI is also useful for detecting small abscesses within the inflamed region (Fig. 12B).[57] In addition, MRI is useful in assessing abscess formation in the intracranial and nasopharyngeal regions as well as the spread of infection to the surrounding structures including the cavernous sinus.[12,56]

Acquired cholesteatoma

Cholesteatomas are benign collections of keratinized squamous epithelium in the middle ear. Chronic and recurrent otolaryngologic infections and inflammations are associated with the formation of cholesteatoma as a complication. MRI is characterized by high signal on non-echoplanar (non-EP) DWI and low signal on T1WI, and these findings are also useful in evaluating the presence of mastoid extension of cholesteatoma (Fig. 13A, B).[58] In particular, non-EP DWI for the detection of middle ear cholesteatoma has a very high sensitivity and specificity of 0.91 and 0.92, respectively.[59] There are reports that it is useful in differentiating cholesteatoma from non-cholesteatoma (mean 0.87 vs 1.87 × $10^{-3}$$mm^2$/s), and in predicting the risk of recurrence after surgery (less than mean 1.00 × $10^{-3}$$mm^2$/s) based on

ADC values derived from DWI(Fig. 13C).[60,61] Recent studies have reported the utility of temporal subtraction CT images in evaluating for recurrence and extension of middle ear cholesteatoma into the mastoid region with a sensitivity of 0.93 and specificity of 1.00 (Fig. 14).[49,50] Fusion imaging of DWI (excellent for lesion detection) and CT/MRI (excellent for anatomical evaluation) has been shown to improve image interpretation of middle ear cholesteatoma (Fig. 15).[62]

Labyrinthitis

Labyrinthitis is characterized by inflammation and infection of the inner ear, usually caused by viral infections, and rarely by bacterial infections.[12] The key imaging finding is enhancement of the membranous labyrinth on post-contrast high-resolution T1WI.[12] Ramsey Hunt syndrome (herpes zoster oticus) is an entity that involves both the facial nerve and the membranous labyrinth. Post-contrast T1WI shows enhancement in the membranous labyrinth, and along the course of the facial nerve within the labyrinthine segment and the internal auditory meatus (Fig. 16).[12] Labyrinthitis ossificans shows characteristic findings of decreased or absent signal compared to normal inner ear fluid on high-resolution T2WI (Fig. 17),[12,63] with MRI being more sensitive than CT in identifying the fibrotic stage.[12,56]

Facial neuropathies

Facial nerve palsy (Bell's palsy) is the most common cause of acute peripheral facial nerve dysfunction, with the etiology attributed to inflammation and edema, often related to viral infection.[64] Bell's palsy usually shows homogeneous enhancement of the facial nerve on post-contrast T1WI (Fig. 18), particularly in segments medial to the geniculate ganglion and/or asymmetric enhancement in the geniculate and lateral segments, where enhancement per se may be a normal finding.[65] There is a recent report that Bell's palsy has a higher incidence of mastoid fluid retention on MRI than Ramsey-Hunt syndrome, which may be an additional finding in differentiating the two entities.[66]

C. Pharynx

Peritonsillar abscess

Peritonsillar abscess results from tonsillitis. In uncomplicated acute tonsillitis, imaging is usually not required. Post-contrast T1WI shows peritonsillar abscess as a localized fluid collection with enhancement of the margins, and DWI shows internal diffusion restriction (Fig. 19).[12] In emergencies, MRI of the head and neck, although not usually the first choice, can provide an accurate assessment of the extent of abscess formation and the extent of deep neck spread, including the parapharyngeal and retropharyngeal spaces.[12,67]

D. Deep neck

The main locations of deep neck infection include the sublingual, parapharyngeal, perivertebral, masticator, and parotid spaces.[68] In the deep neck region, it is clinically important to differentiate between cellulitis and abscess and to assess the extent of abscess extension. MRI has been reported to be superior to CT in clearly visualizing lesions, assessing extension, and identifying the origin of infection.[69] MRI also has a very high diagnostic accuracy of 0.96 for abscesses[4]. On MRI, cellulitis shows diffuse swelling and edema with increased signal on fat-suppressed T2WI and STIR (Fig. 20A, 21A), and enhancement on post-contrast T1WI. Abscess is seen as a localized non-enhancing area with enhancing margins on post-contrast T1WI with associated surrounding cellulitis. The cellulitis shows high ADC values compared to the abscess which shows low ADC values (Fig. 20B, 21B).[70] The diagnostic performance of DWI and contrast-enhanced MRI is equivalent in the detection of abscesses.[71] MR venography is useful in detecting internal jugular vein thrombophlebitis, o including Lemierre's syndrome.[72] DWI can also detect thrombophlebitis due to high signal from intraluminal thrombus.[70] Low keV (40 keV) virtual monochromatic image and iodine mapping derived from dual-energy CT have recently been reported to be useful in the evaluation of deep neck abscess (Fig. 22).[73]

E. Oral cavity

Periapical/periodontal disease, osteomyelitis of the jaw

Odontogenic infections are the most common form of inflammatory disease of the head and neck.[74] Acute osteomyelitis of the jaw shows low signal intensity on T1WI and high signal intensity on T2WI, whereas chronic osteomyelitis of the jaw shows low signal intensities on both T1WI and T2WI.[75] In particular, STIR is effective in detecting osteomyelitis of the jaw and assessing surrounding soft tissue inflammation (Fig. 23A).[76] It has been reported that the ADC value derived from DWI is useful in the quantitative assessment of mandibular osteomyelitis (higher ADC [cut-off value, 0.98] indicates osteomyelitis) (Fig. 23B),[77] and that the ADC value of odontogenic abscesses is very low (mean 0.67×10^{-3} mm^2/s), which is useful in differentiating them from other maxillofacial diseases.[78] MR bone imaging[44,45] may add new value to the morphologic evaluation of osteomyelitis of the jaw (Fig. 24). Dynamic maneuvers for evaluating lesions, such as puffed-cheek distension combined with breath-holding, can better visualize the oral cavity where anatomical structures are in close proximity[79] and may improve imaging of oral infections and abscesses.

Artifacts associated with dental treatment

Dental fillings as a treatment can cause severe beam-hardening artifacts on CT , making detailed evaluation of the oral cavity and oropharyngeal region difficult in many cases.[80] MRI is a superior imaging modality for imaging oral cavity lesions with fewer

artifacts compared to CT.[6] Known artifact reduction methods include the use of bite blocks and tilting the CT gantry or patient head.[81] Improvements in the evaluation of intraoral CT images have been reported with new technologies such as the metal artefact reduction (MAR) algorithm for CT artifact reduction(Fig. 25A, B).[82,83] Virtual monochromatic imaging at a high energy level (derived from dual-energy CT) has also been shown to reduce metal artifacts associated with dental hardware compared to conventional CT[84] (Fig. 26). In addition, the combination of the MAR algorithm and dual-energy CT-derived virtual monochromatic imaging to reduce dental metal artifacts has recently been reported to be beneficial in this context.[85] There is additional developing evidence that subtraction iodine imaging, which is an application of the subtraction CT technique, can reduce intraoral metal artifacts by subtracting artifacts (Fig. 25C).[86]

F. Salivary Glands

Infections of the salivary glands can be acute, recurrent or chronic and are related to obstructive mechanisms such as salivary stones, and can be either bacterial or viral in etiology.[87] On MRI, sialadenitis is seen as diffuse enlargement of the glands with high signal on T2WI and STIR,[87] and enhancement with enlarged glands on post contrast T1WI. In the case of acute bacterial sialadenitis, DWI can be used to detect early stage or small abscess formation with high sensitivity compared to conventional imaging.[57] DWI has shown high

diagnostic performance in detecting changes in the salivary glands and may be useful in the evaluation of sialadenitis (Fig. 27).[88] It has been reported that early pathologic changes in Sjögren's syndrome can result in a definite increase in ADC values even when they cannot be visualized with conventional MRI, and may be useful in differentiating from infectious sialadenitis.[89] Virtual unenhanced images derived from dual energy CT may be an alternative to conventional non-contrast CT in the detection of sialolithiasis[3] (Fig. 28).

Conclusion

In this article, we have reviewed important head and neck infections in a region-by-region approach, including features derived from conventional imaging as well as contemporary emerging technologies. By reading this article, we hope that the readers gain a better understanding of the role of various imaging modalities in the workup of head and neck infections.

Acknowledgements and Disclosure

The authors would like to thank Dr. Koichi Masuda, Dr. Hiroaki Fujioka, Mr. Hisashi Kitagawa, Mr. Tomoki Natsuizaka, Dr. Hiroya Ojiri, Dr. Takashi Hiyama, Dr. Hirofumi Kuno, John Kim, and Toshio Moritani for providing us with precious figures and advices. This article was presented in part at the 108th annual meeting of the Radiological

Society of North America (RSNA) in Chicago, 2022. It received a Cum Laude for educational exhibit.

The authors declare that they have no competing interests.

References

1. Hegde AN, Mohan S, Pandya A, et al. Imaging in Infections of the Head and Neck. Neuroimaging Clin N Am 2012;22:727–54.

2. Hurley MC, Heran MKS. Imaging studies for head and neck infections. Infect Dis Clin North Am 2007;21:305–53.

3. Beland B, Levental M, Srinivasan A, et al. Practice variations in salivary gland imaging and utility of virtual unenhanced dual energy CT images for the detection of major salivary gland stones. Acta radiol 2019;60:1144–52.

4. Nurminen J, Velhonoja J, Heikkinen J, et al. Emergency neck MRI: feasibility and diagnostic accuracy in cases of neck infection. Acta radiol 2021;62:735–42.

5. Muñoz A, Castillo M, Melchor MA, et al. Acute neck infections: prospective comparison between CT and MRI in 47 patients. J Comput Assist Tomogr 2001;25:733-41.

6. Lenz M, Greess H, Baum U, et al. Oropharynx, oral cavity, floor of the mouth: CT and MRI. Eur J Radiol 2000;33:203–15.

7. Hu L, Wei L, Wang S, et al. Better lesion conspicuity translates into improved prostate cancer detection: comparison of non-parallel-transmission-zoomed-DWI with conventional-DWI. Abdom Radiol 2021;46:5659–68.

8. Medvedeva N, Radcliffe C, Malinis M, et al. Real-world assessment of the clinical utility of whole body 18F-FDG PET/CT in the diagnosis of infection. PLoS One 2022;17:e0277403.

9. Goel R, Moore W, Sumer B, et al. Clinical practice in PET/CT for the management of head and neck squamous cell cancer. AJR Am J Roentgenol 2017;209:289–303.

10. Stern Shavit S, Bernstine H, Sopov V, et al. FDG-PET/CT for diagnosis and follow-up of necrotizing (malignant) external otitis. Laryngoscope 2019;129:961–6.

11. Dijkstra GW, Glaudemans AWJM, Erba PA, et al. Relationship between 18F-FDG uptake in the oral cavity, recent dental treatments, and oral inflammation or infection: a retrospective study of patients with suspected endocarditis. Diagnostics 2020;10:625.

12. Thayil N, Chapman MN, Saito N, et al. Magnetic resonance imaging of acute head and neck infections. Magn Reson Imaging Clin N Am 2016;24:345–67.

13. LeBedis CA, Sakai O. Nontraumatic orbital conditions: diagnosis with CT and MR imaging in the emergent setting. RadioGraphics 2008;28:1741–53.

14. Jyani R, Ranade D, Joshi P. Spectrum of orbital cellulitis on magnetic resonance imaging. Cureus 2020;12:e966315.

15. Dankbaar JW, van Bemmel AJM, Pameijer FA. Imaging findings of the orbital and intracranial complications of acute bacterial rhinosinusitis. Insights Imaging 2015;6:509–18.

16. Nguyen VD, Singh AK, Altmeyer WB, et al. Demystifying orbital emergencies: a pictorial review. Radiographics 2017;37:947–62.

17. Sepahdari AR, Aakalu VK, Kapur R, et al. MRI of orbital cellulitis and orbital abscess: the role of diffusion-weighted imaging. AJR Am J Roentgenol 2009;193:244-50.

18. Brucker JL, Gentry LR. Imaging of head and neck emergencies. Radiol Clin North Am 2015;53:215-52.

19. Sotoudeh H, Shafaat O, Aboueldahab N, et al. Superior ophthalmic vein thrombosis: what radiologist and clinician must know? Eur J Radiol Open 2019;6:258–64.

20. Yıldız ME, Ozcan UA, Turk A, et al. Diffusion-weighted MR imaging findings of cortical vein thrombosis at 3 T. Clin Neuroradiol 2015;25:249–56.

21. Aribandi M, McCoy VA, Bazan C. Imaging features of invasive and noninvasive fungal sinusitis: a review. Radiographics 2007;27:1283–96.

22. Eggesbø HB. Radiological imaging of inflammatory lesions in the nasal cavity and paranasal sinuses. Eur Radiol 2006;16:872–88.

23. Germiller JA, Monin DL, Sparano AM, et al. Intracranial complications of sinusitis in children and adolescents and their outcomes. Arch Otolaryngol Head Neck Surg 2006;132:969–76.

24. Kamran S, Bener AB, Alper D, et al. Role of fluid-attenuated inversion recovery in the diagnosis of meningitis: comparison with contrast-enhanced magnetic resonance imaging. J Comput Assist Tomogr 2004;28:68-72.

25. Vaswani AK, Nizamani WM, Ali M, et al. Diagnostic accuracy of contrast-enhanced FLAIR magnetic resonance imaging in diagnosis of meningitis correlated with CSF analysis. ISRN Radiol 20;2014:578986.

26. Toh CH, Wei K-C, Chang C-N, et al. Differentiation of pyogenic brain abscesses from necrotic glioblastomas with use of susceptibility-weighted imaging. AJNR Am J Neuroradiol 2012;33:1534–8.

27. Ni Mhurchu E, Ospina J, Janjua AS, et al. Fungal rhinosinusitis: a radiological review with intraoperative correlation. Can Assoc Radiol J 2017;68:178–86.

28. Ilica AT, Mossa-Basha M, Maluf F, et al. Clinical and radiologic features of fungal diseases of the paranasal sinuses. J Comput Assist Tomogr 2012;36:570-6.

29. Meng Y, Zhang L, Piao Y, et al. The use of magnetic resonance imaging in differential diagnosis of allergic fungal sinusitis and eosinophilic mucin rhinosinusitis. J Thorac Dis 2019;11:3569–77.

30. Sasaki M, Eida S, Sumi M, et al. Apparent diffusion coefficient mapping for sinonasal diseases: differentiation of benign and malignant lesions. AJNR Am J Neuroradiol 2011;32:1100–6.

31. Seo Y-J, Kim J, Kim K, et al. Radiologic characteristics of sinonasal fungus ball: an analysis of 119 cases. Acta Radiol 2011;52:790–5.

32. Kim SC, Ryoo I, Shin JM, et al. MR findings of fungus ball: significance of high signal intensity on T1-weighted images. J Korean Med Sci 2020;35:e22.

33. Mossa-basha M, Maluf F. The many faces of fungal disease of the paranasal sinuses: CT and MRI findings. Diagn Interv Radiol 2013;19:195-200.

34. Smith SM, Thelen JC, Bhatt AA, et al. Facial swelling for the emergency radiologist-typical and atypical causes. Emerg Radiol 2021;28:177-83.

35. Safder S, Carpenter JS, Roberts TD, et al. The “Black Turbinate” sign: an early MR imaging finding of nasal mucormycosis. AJNR Am J Neuroradiol 2010;31:771–4.

36. Li Z, Wang X, Jiang H, et al. Chronic invasive fungal rhinosinusitis vs sinonasal squamous cell carcinoma : the differentiating value of MRI. Eur Radiol 2020;30:4466-74..

37. Choi YR, Kim J, Min HS, et al. Acute invasive fungal rhinosinusitis: MR imaging features and their impact on prognosis. Neuroradiology 2018;60:715–23.

38. Vaidyanathan S, Lingam RK. Imaging of acute and chronic skull base infection. Neuroimaging Clin N Am 2021;31:571–98.

39. Courson AM, Vikram HR, Barrs DM. What are the criteria for terminating treatment for necrotizing (malignant) otitis externa? Laryngoscope 2014;124:361–2.

40. van Kroonenburgh AMJL, van der Meer WL, Bothof RJP, et al. Advanced imaging techniques in skull base osteomyelitis due to malignant otitis externa. Curr Radiol Rep 2018;6:3.

41. Álvarez Jáñez F, Barriga LQ, Iñigo TR, et al. Diagnosis of skull base osteomyelitis. RadioGraphics 2021;41:156–74.

42. Ozgen B, Oguz KK, Cila A. Diffusion MR imaging features of skull base osteomyelitis compared with skull base malignancy. AJNR Am J Neuroradiol 2011;32:179–84.

43. Baba A, Kurokawa R, Kurokawa M, et al. Dynamic contrast-enhanced MRI parameters and normalized ADC values could aid differentiation of skull base osteomyelitis from nasopharyngeal cancer. AJNR Am J Neuroradiol 2023;44:74-8.

44. Wiesinger F, Sacolick LI, Menini A, et al. Zero TE MR bone imaging in the head. Magn Reson Med 2016;75:107–14.

45. Jans LBO, Chen M, Elewaut D, et al. MRI-based synthetic CT in the detection of structural lesions in patients with suspected sacroiliitis: comparison with MRI. Radiology 2021;298:343–9.

46. Hiyama T, Kuno H, Sekiya K, et al. Bone subtraction iodine imaging using area detector CT for evaluation of skull base invasion by nasopharyngeal carcinoma. AJNR Am J Neuroradiol 2019;40:135–41.

47. Al-Noury K, Lotfy A. Computed tomography and magnetic resonance imaging findings before and after treatment of patients with malignant external otitis. Eur Arch Otorhinolaryngol 2011;268:1727-34..

48. Cherko M, Nash R, Singh A, et al. Diffusion-weighted magnetic resonance imaging as a novel imaging modality in assessing treatment response in necrotizing otitis externa. Otol Neurotol 2016;37:704-7.

49. Baba A, Kurokawa R, Kurokawa M, et al. Preoperative prediction for mastoid extension of middle ear cholesteatoma using temporal subtraction serial HRCT studies. Eur Radiol 2022;32:3631-8.

50. Baba A, Matsushima S, Fukuda T, et al. Improved assessment of middle ear recurrent/residual cholesteatomas using temporal subtraction CT. Jpn J Radiol 2022;40:271–8.

51. Baba A, Kurihara S, Kurokawa R, et al. Comparative evaluation of temporal subtraction computed tomography and non-echoplanar diffusion-weighted imaging for the mastoid extension of middle ear cholesteatoma. Auris Nasus Larynx 2022;49:956-63.

52. Chengazi H V, Desai A, Bhatt AA. Emergency radiologic approach to mastoid air cell fluid. Emerg Radiol 2021;28:633–40.

53. Saat R, Laulajainen-Hongisto AH, Mahmood G, et al. MR imaging features of acute mastoiditis and their clinical relevance. AJNR Am J Neuroradiol 2015;36:361–7.

54. Lo ACC, Nemec SF. Opacification of the middle ear and mastoid: imaging findings and clues to differential diagnosis. Clin Radiol 2015;70:e1–13.

55. Saat R, Kurdo G, Laulajainen-Hongisto A, et al. Detection of coalescent acute mastoiditis on MRI in comparison with CT. Clin Neuroradiol 2021;31:589–97.

56. Campion T, Taranath A, Pinelli L, et al. Imaging of temporal bone inflammations in children: a pictorial review. Neuroradiology 2019;61:959–70.

57. Boucher F, Liao E, Srinivasan A. Diffusion-weighted imaging of the head and neck (including temporal bone). Magn Reson Imaging Clin N Am 2021;29:205–32.

58. Baba A, Kurihara S, Fukuda T, et al. Non-echoplanar diffusion weighed imaging and T1-weighted imaging for cholesteatoma mastoid extension. Auris Nasus Larynx 2021;48:846-51.

59. Lingam ÃRK, Bassett P. A meta-analysis on the diagnostic performance of non-echoplanar diffusion-weighted imaging in detecting middle ear cholesteatoma : 10 years on. Otol Neurotol 2017;38:521-528.

60. Russo C, Elefante A, Cavaliere M, et al. Apparent diffusion coefficients for predicting primary cholesteatoma risk of recurrence after surgical clearance. Eur J Radiol 2020;125:108915..

61. Fan X, Liu Z, Ding C, et al. The value of turbo spin-echo diffusion-weighted imaging apparent diffusion coefficient in the diagnosis of temporal bone cholesteatoma. Clin Radiol 2019;74:977.e1-977.e7.

62. Fan X, Ding C, Liu Z. Comparison of the utility of high-resolution CT-DWI and T2WI-DWI fusion images for the localization of cholesteatoma. AJNR Am J Neuroradiol 2022;43:1029–35.

63. Booth TN, Roland P, Kutz JW, et al. High-resolution 3-D T2-weighted imaging in the diagnosis of labyrinthitis ossificans: emphasis on subtle cochlear involvement. Pediatr Radiol 2013;43:1584–90.

64. Zhang W, Xu L, Luo T, et al. The etiology of Bell's palsy: a review. J Neurol 2020;267:1896–905.

65. Warne R, Carney OM, Wang G, et al. Enhancement patterns of the normal facial nerve on three-dimensional T1W fast spin echo MRI. Br J Radiol 2021;94:20201025.

66. Choi JW, Lee J, Lee D-H, et al. Mastoid effusion on temporal bone MRI in patients with Bell's palsy and Ramsay Hunt syndrome. Sci Rep 2021;11:3127.

67. Heikkinen J, Nurminen J, Velhonoja J, et al. MRI findings in acute tonsillar infections. AJNR Am J Neuroradiol 2022;43:286–91.

68. Maroldi R, Farina D, Ravanelli M, et al. Emergency imaging assessment of deep neck space infections. Semin Ultrasound CT MR 2012;33:432–42.

69. Babu VR, Ikkurthi S, Perisetty DK, et al. A prospective comparison of computed tomography and magnetic resonance imaging as a diagnostic tool for maxillofacial space infections. J Int Soc Prev Community Dent 2018;8:343–8.

70. Norris CD, Quick SE, Parker JG. Diffusion MR imaging in the head and neck principles and applications. Neuroimaging Clin N Am 2020;30:261–82.

71. Chun CW, Jung J-Y, Baik JS, et al. Detection of soft-tissue abscess: Comparison of diffusion-weighted imaging to contrast-enhanced MRI. J Magn Reson Imaging 2018;47:60–8.

72. Orman G, Kralik SF, Desai N, et al. Imaging of paranasal sinus infections in children: a review. J Neuroimaging 2020;30:572–86.

73. Hattori Y, Azuma M, Nakada H, et al. Usefulness of virtual monochromatic images and iodine maps derived from dual-energy computed tomography for diagnosing deep neck abscesses. J Comput Assist Tomogr 2021; 45:625-8.

74. Parhiscar A, Har-El G. Deep neck abscess: a retrospective review of 210 cases. Ann Otol Rhinol Laryngol 2001;110:1051–4.

75. Mardini S, Gohel A. Imaging of odontogenic infections. Radiol Clin North Am 2018;56:31-44.

76. Lee K, Kaneda T, Mori S, et al. Magnetic resonance imaging of normal and osteomyelitis in the mandible: assessment of short inversion time inversion recovery sequence. Oral Surg Oral Med Oral Pathol Oral Radiol 2003;96:499-507.

77. Muraoka H, Hirahara N, Ito K, et al. Efficacy of diffusion-weighted magnetic resonance imaging in the diagnosis of osteomyelitis of the mandible. Oral Surg Oral Med Oral Pathol Oral Radiol 2022;133:80-7.

78. Oda T, Sue M, Sasaki Y, et al. Diffusion-weighted magnetic resonance imaging in oral and maxillofacial lesions: preliminary study on diagnostic ability of apparent diffusion coefficient maps. Oral Radiol 2018;34:224–8.

79. Erdogan N, Bulbul E, Songu M, et al. Puffed-cheek computed tomography: a dynamic maneuver for imaging oral cavity tumors. Ear Nose Throat J 2012;91:383–6.

80. Baba A, Ojiri H, Ogane S, et al. Usefulness of contrast-enhanced CT in the evaluation of depth of invasion in oral tongue squamous cell carcinoma: comparison with MRI. Oral Radiol 2021;37:86–94.

81. Marcus RP, Morris JM, Matsumoto JM, et al. Implementation of iterative metal artifact reduction in the pre-planning-procedure of three-dimensional physical modeling. 3D Print Med 2017;3:5.

82. Feldhaus F, Böning G, Jonczyk M, et al. Metallic dental artifact reduction in computed tomography (Smart MAR): Improvement of image quality and diagnostic confidence in patients with suspected head and neck pathology and oral implants. Eur J Radiol 2019;118:153–60.

83. Troeltzsch D, Shnayien S, Heiland M, et al. Detectability of head and neck cancer via new computed tomography reconstruction tools including Iterative reconstruction and metal artifact reduction. Diagnostics (Basel) 2021;11:2154.

84. Liao E, Srinivasan A. Applications of dual-energy computed tomography for artifact reduction in the head, neck, and spine. Neuroimaging Clin N Am 2017;27:489–97.

85. Schmidt AMA, Grunz J-P, Petritsch B, et al. Combination of iterative metal artifact reduction and virtual monoenergetic reconstruction using split-filter dual-energy CT in patients with dental artifact on head and neck CT. AJR Am J Roentgenol 2022;218:716-27.

86. Hiyama T, Kuno H, Sekiya K, et al. Subtraction iodine imaging with area detector CT to improve tumor delineation and measurability of tumor size and depth of invasion in tongue squamous cell carcinoma. Jpn J Radiol 2022;40:167-76.

87. Jeffery DT, Jeffery CC, Kelly HR. Chew on this: emergency imaging of the oral cavity and salivary glands—what the clinician really needs to know. Semin Ultrasound CT MR 2019;40:104–15.

88. Araujo JP, Terra GTC, Cortes ARG, et al. A comparison of conventional and diffusion-weighted magnetic resonance imaging in the diagnosis of sialadenitis and pleomorphic adenoma. Oral Surg Oral Med Oral Pathol Oral Radiol 2019;127:451-457.

89. Ding C, Xing X, Guo Q, et al. Diffusion-weighted MRI findings in Sjögren's syndrome: a preliminary study. Acta Radiol 2016;57:691–700.

Figure Legends

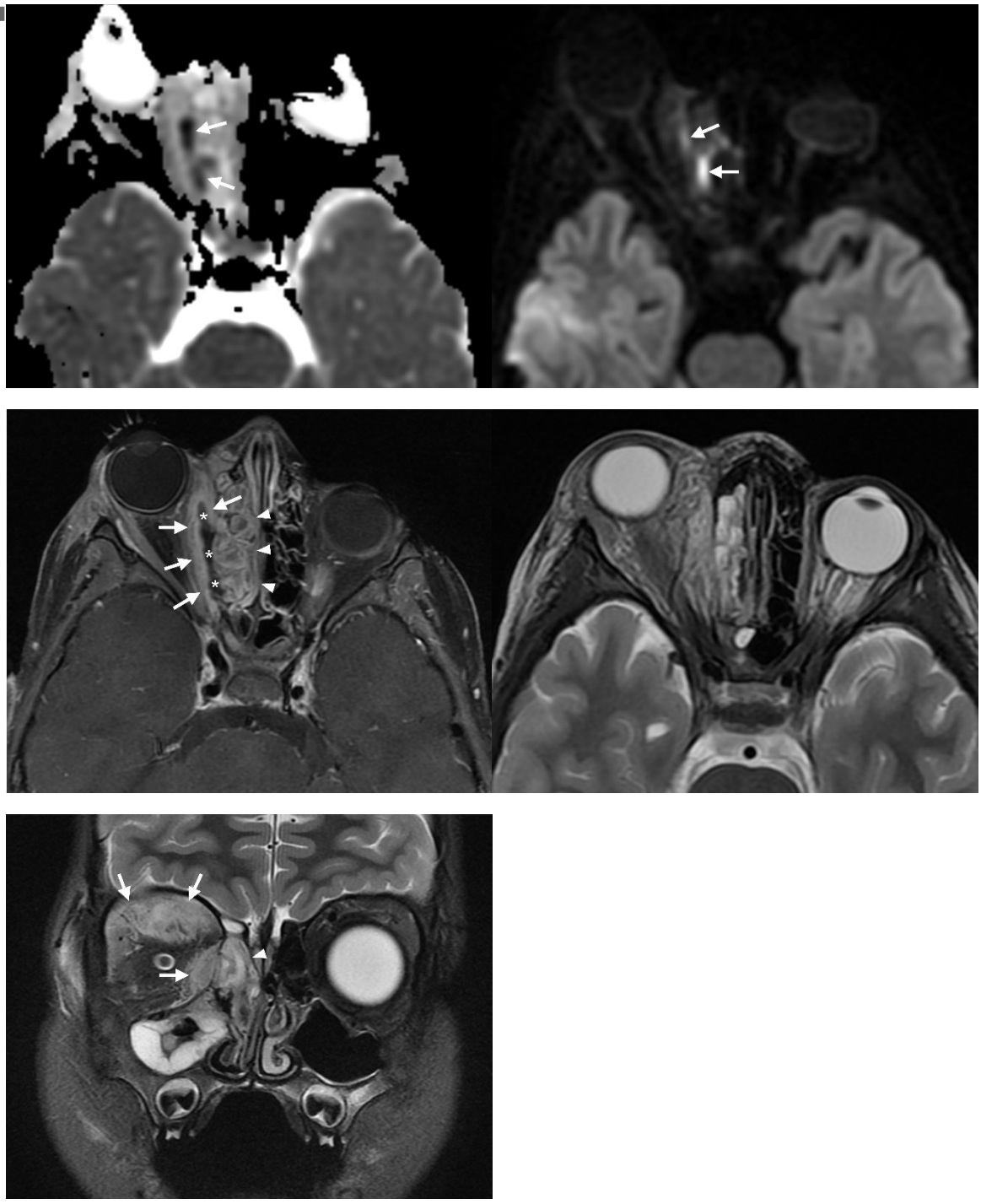

Figure 1. 4-year-old male with orbital cellulitis associated with ethmoid sinusitis. Fat-suppressed T2-weighted coronal images (A) show high signal intensities (arrows) consistent with cellulitis secondary to right ethmoid sinusitis (arrowheads). Conventional T2-weighted axial image (B) shows high signal intensities in the bilateral infraorbital regions, complicating detailed evaluation of inflammatory spread. Contrast-enhanced fat-suppressed T1-weighted image (C) shows irregular enhancement at the margin (arrows) and lack of enhancement (*) in the right orbital subperiosteum. There is enhancement (arrowheads) with mucosal thickening of the right ethmoid air cells. The right orbital lesion shows high signal (arrows) on diffusion-weighted imaging (D) and low signal (arrows) on apparent diffusion coefficient (ADC) map (E), indicating diffusion restriction consistent with abscess formation. The ADC value is $0.56 \times 10^{-3} mm^2/s$.

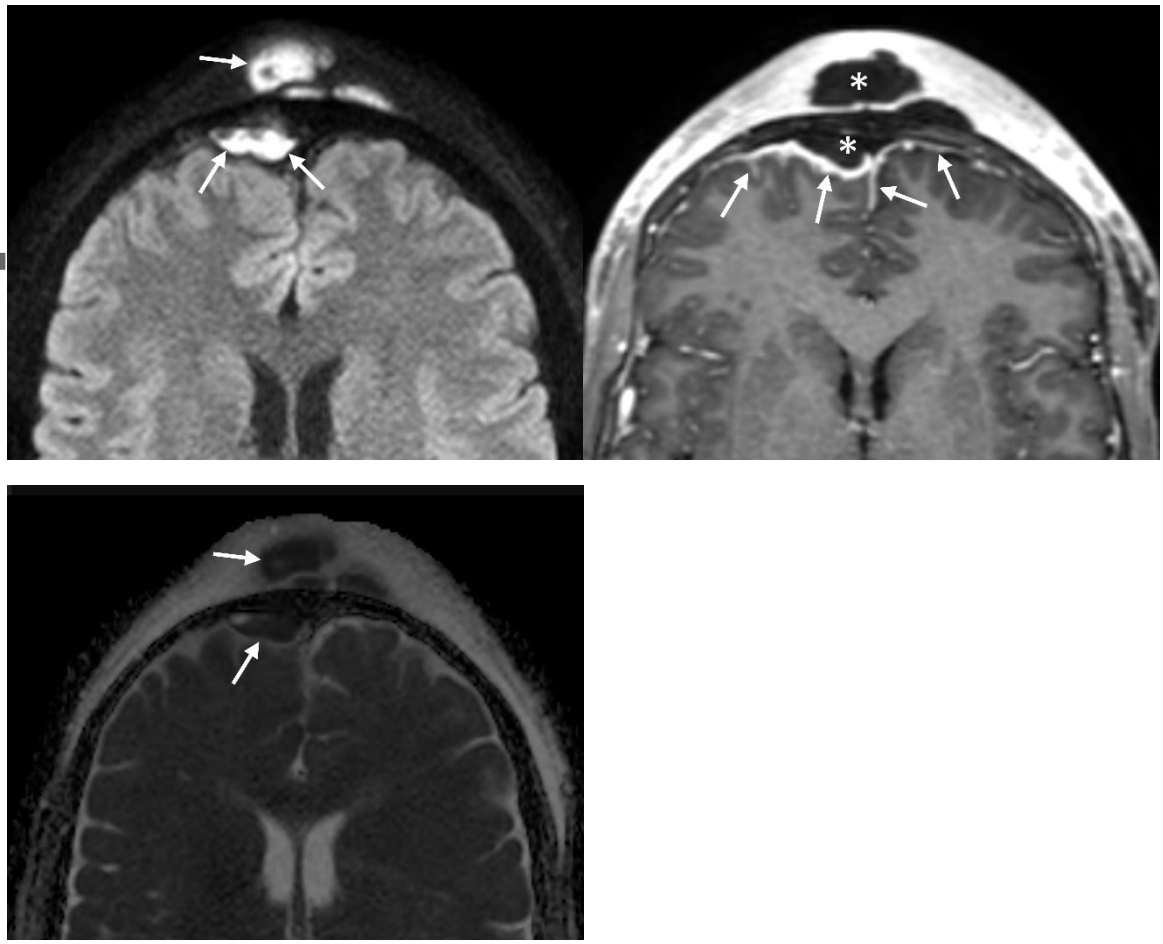

Figure 2. 24-year-old male with intracranial subdural empyema and meningitis associated with frontal sinusitis. Contrast-enhanced fat-suppressed T1-weighted image (A) shows intracranial subdural and frontal subcutaneous areas of poor enhancement (*) with enhancement at the margins, indicating an abscess. Meningeal thickening (arrows) with enhancement adjacent to the intracranial abscess suggests meningitis. Diffusion-weighted imaging (B) shows high signal intensities (arrows) with the low mean apparent diffusion coefficient value of $0.51 \times 10^{-3} mm^2/s$ (C, arrows), indicating diffusion restriction, consistent with intracranial subdural empyema and frontal subcutaneous abscess (Pott's puffy tumor).

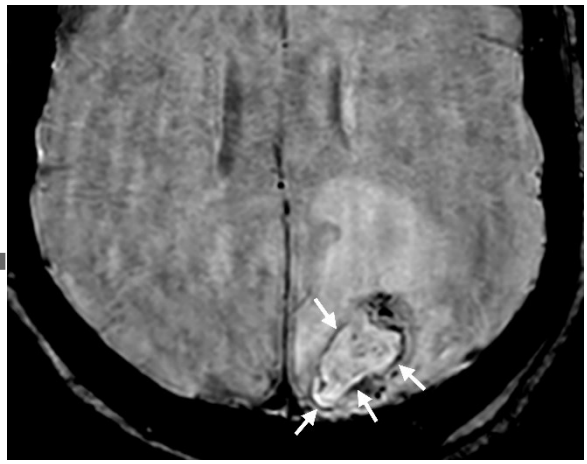

Figure 3. 69-year-old male with brain abscess. Susceptibility-weighted imaging shows double rim sign (surrounded by two concentric rims, with the outer rim showing low signal intensity and the inner rim showing high signal intensity, arrows).

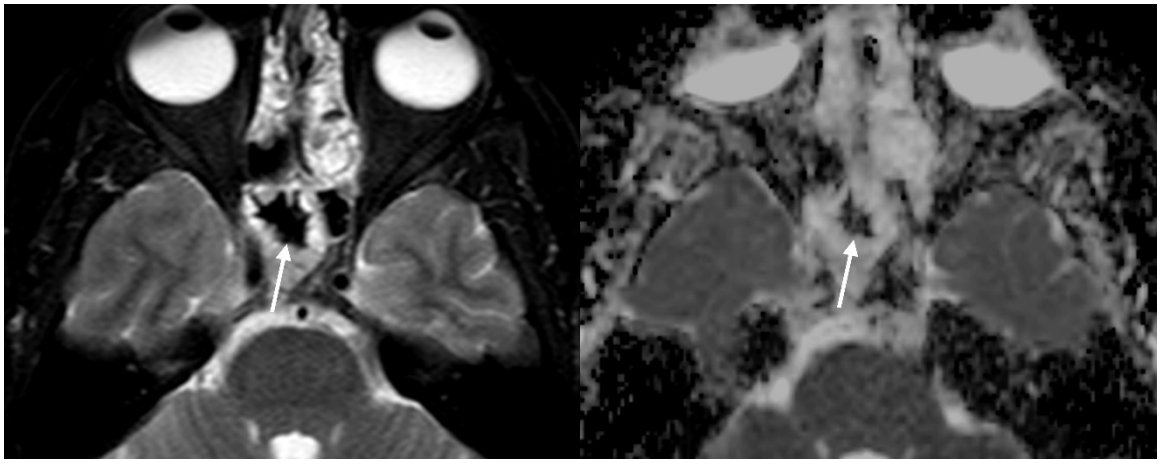

Figure 4. 38-year-old female with allergic fungal rhinosinusitis. Fat-suppressed T2-weighted imaging (A) shows a markedly low signal in the right sphenoid sinus (arrow). The apparent diffusion coefficient value of the lesion was 0.53×10^{-3} mm^2/s (B, arrow).

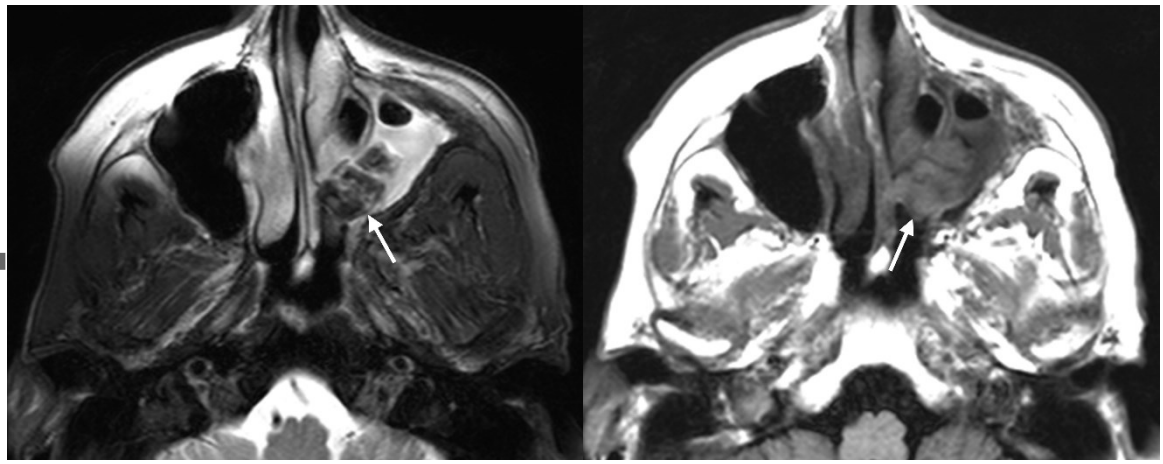

Figure 5. 82-year-old female with a fungus ball in the left maxillary sinus. T2-weighted image (A) shows a nodular structure with low signal intensity in the left maxillary sinus (arrow), consistent with a fungal ball. T1-weighted image (B) shows the fungal ball with high signal intensity (arrow).

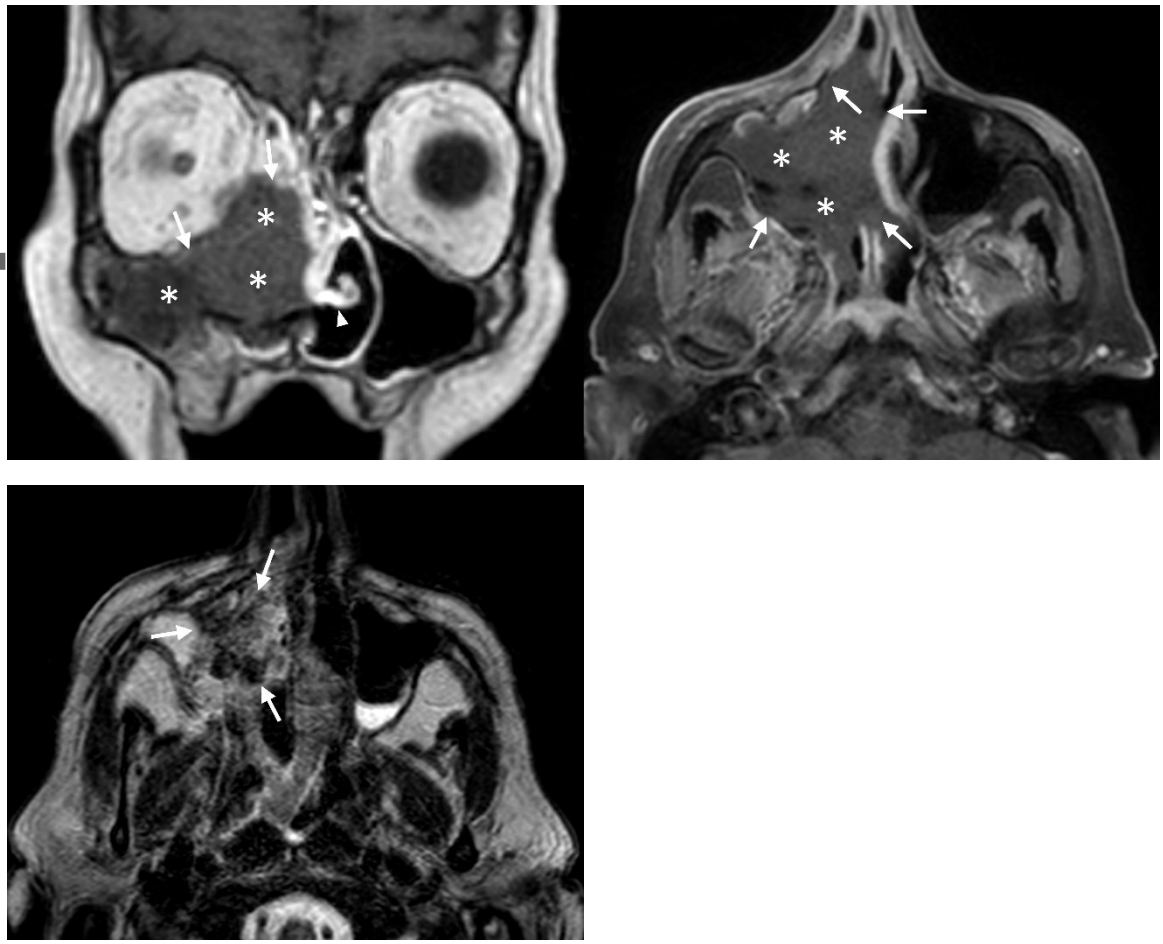

Figure 6. 61-year-old male with invasive fungal rhinosinusitis. Contrast-enhanced T1-weighted image (A, B) shows a non-enhancing lesion (*) from the right maxillary sinus to the nasal cavity and lack of contrast enhancement of the adjacent right maxillary sinus and nasal mucosa and nasal septum (arrows). The normal nasal turbinate (arrowhead) is absent on the right side (black turbinate sign). T2-weighted image (C) shows heterogeneous low-signal intensity (arrows) within the lesion.

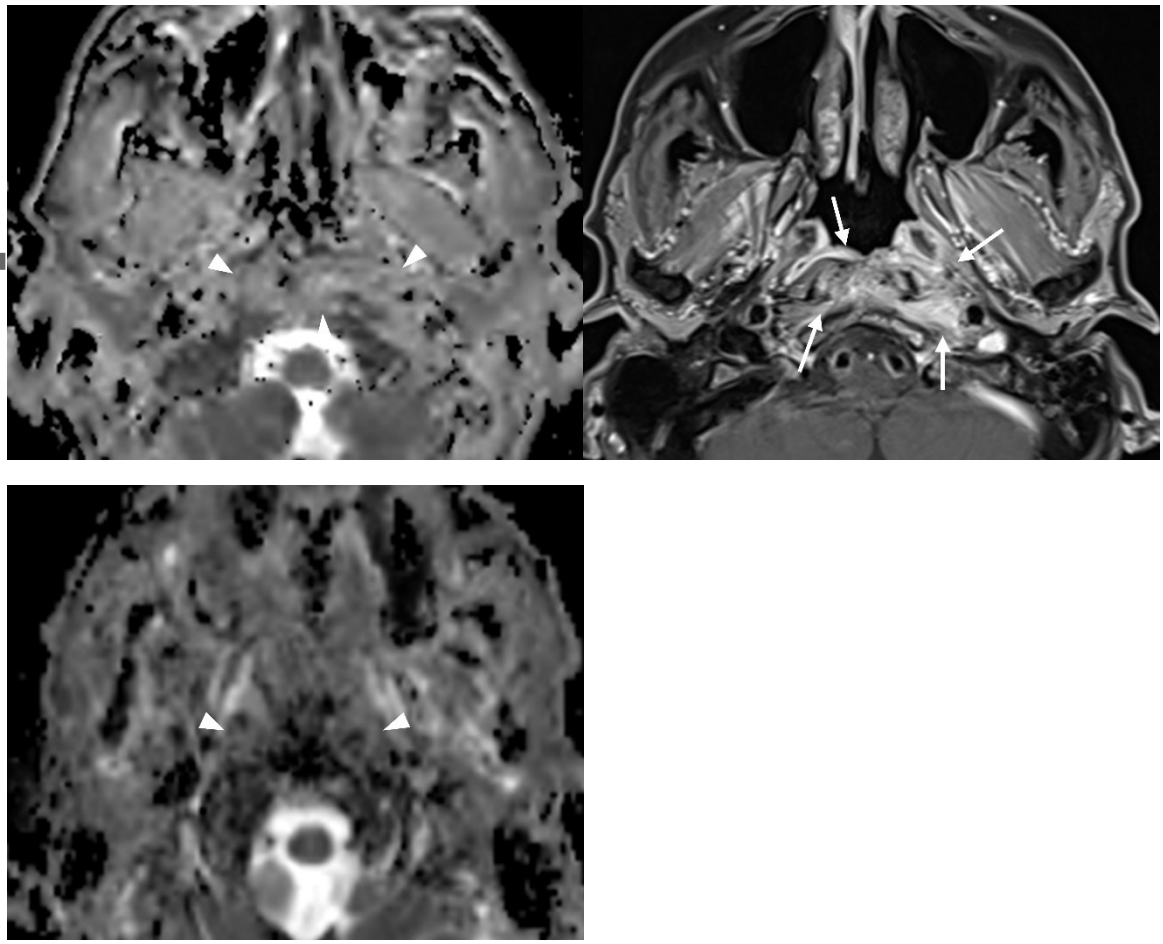

Figure 7. 72-year-old male with skull base osteomyelitis. Post-contrast fat-suppressed T1-weighted image (A) shows ill-defined enhancement (arrows) in the nasopharynx, prevertebral space, and left parapharyngeal space (arrows). The pre-treatment apparent diffusion coefficient (ADC) value is 1.49×10^{-3} mm^2/s (B, arrowheads) and the post-treatment ADC value is 0.94×10^{-3} 10^{-3} mm^2/s (C, arrowheads), and such a reduction of ADC values indicates a good response to treatment.

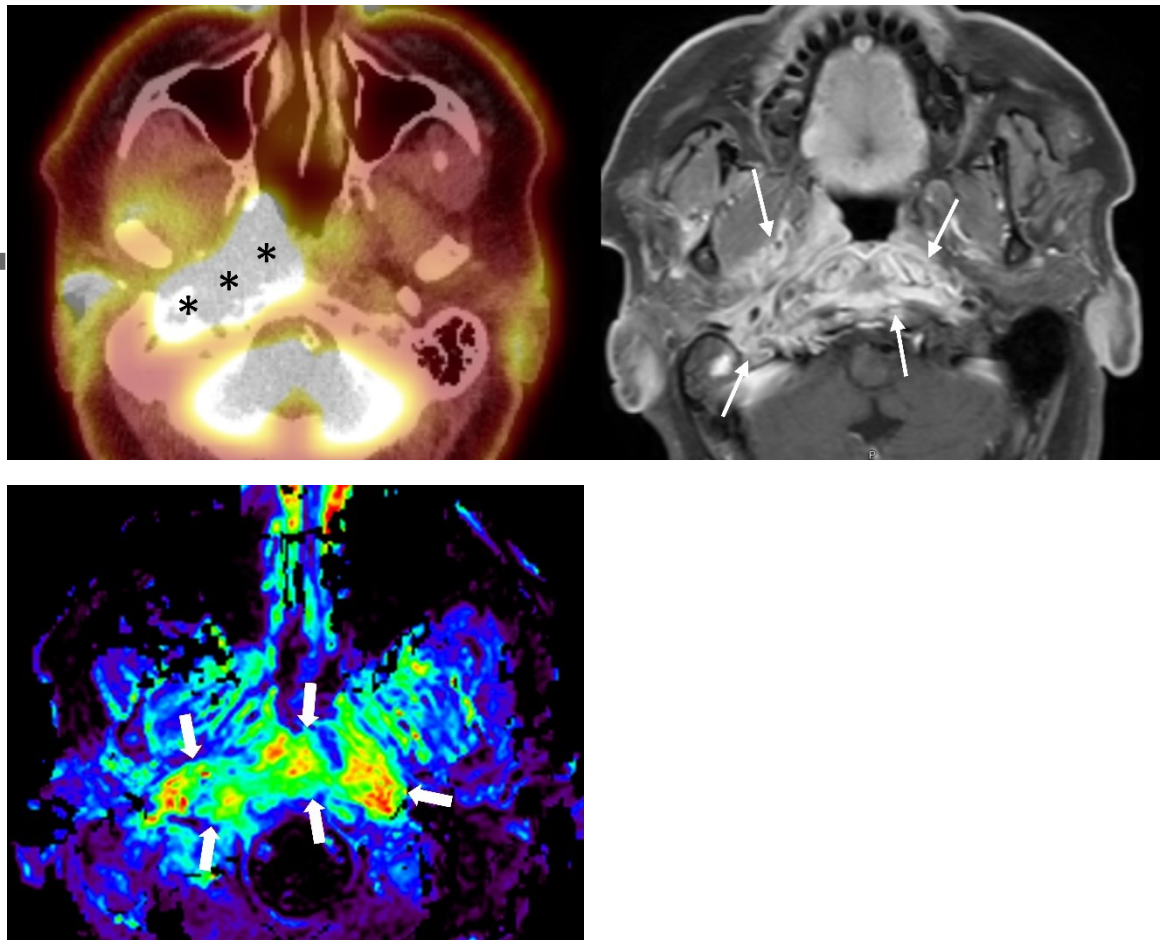

Figure 8. 68-year-old female with necrotizing otitis externa and skull base osteomyelitis. Contrast-enhanced fat-suppressed T1-weighted image (A) shows diffuse heterogeneous enhancement (arrows) consistent with inflammation of the bilateral nasopharynx, skull base, and clivus. ^{18}F-fludeoxyglucose(FDG)-PET/CT (B) shows prominent FDG uptake (*: maximum standardized uptake value max = 18.0) corresponding to the lesion on MRI. Dynamic contrast-enhanced MRI (fraction of the extravascular extracellular space [Ve]: C) also shows increased perfusion (thick arrows) with Ve of 0.54.

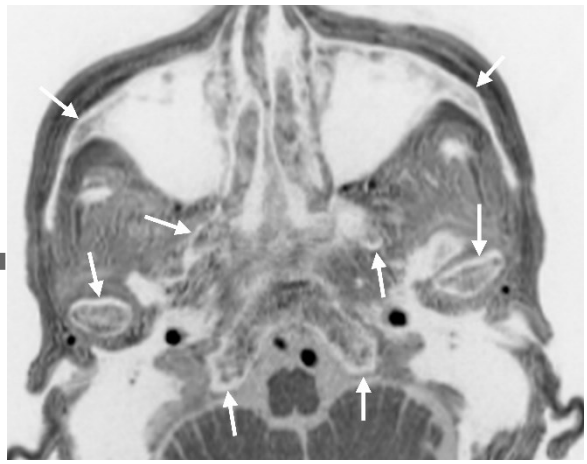

Figure 9. 75–year-old healthy male. MR bone imaging at the level of the skull base clearly shows the bony cortex and trabecula of the clivus, pterygoid process, condylar process, and zygomatic bone (arrows).

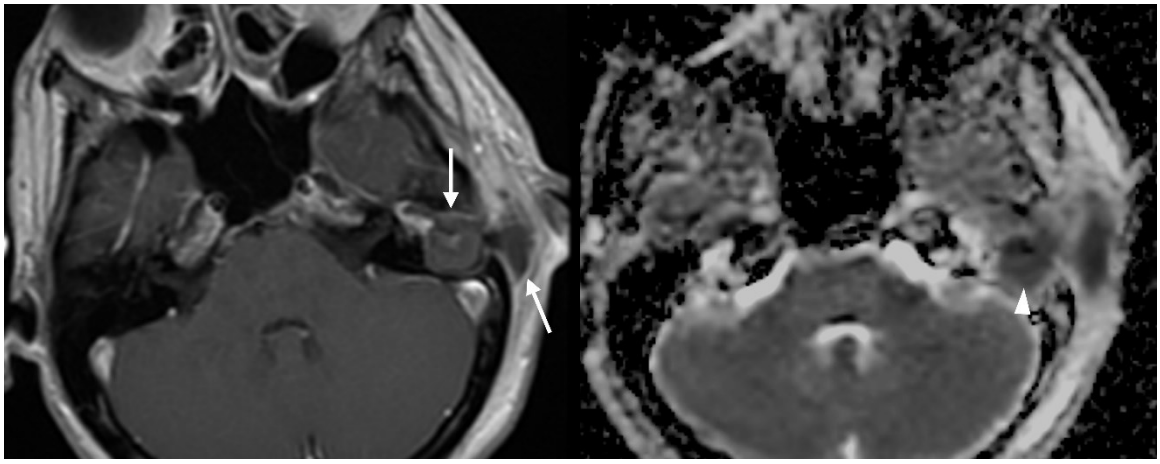

Figure 10. 29-year-old female with complicated coalescent mastoiditis. Post-contrast T1-weighted image (A) shows a hypo-enhancing region from the left mastoid to the adjacent subcutaneous area with an enhancing rim (arrows), consistent with coalescent mastoiditis

associated with subcutaneous and subperiosteal abscesses. The apparent diffusion coefficient value (B, arrowhead) was 0.49×10^{-3} mm^2/s.

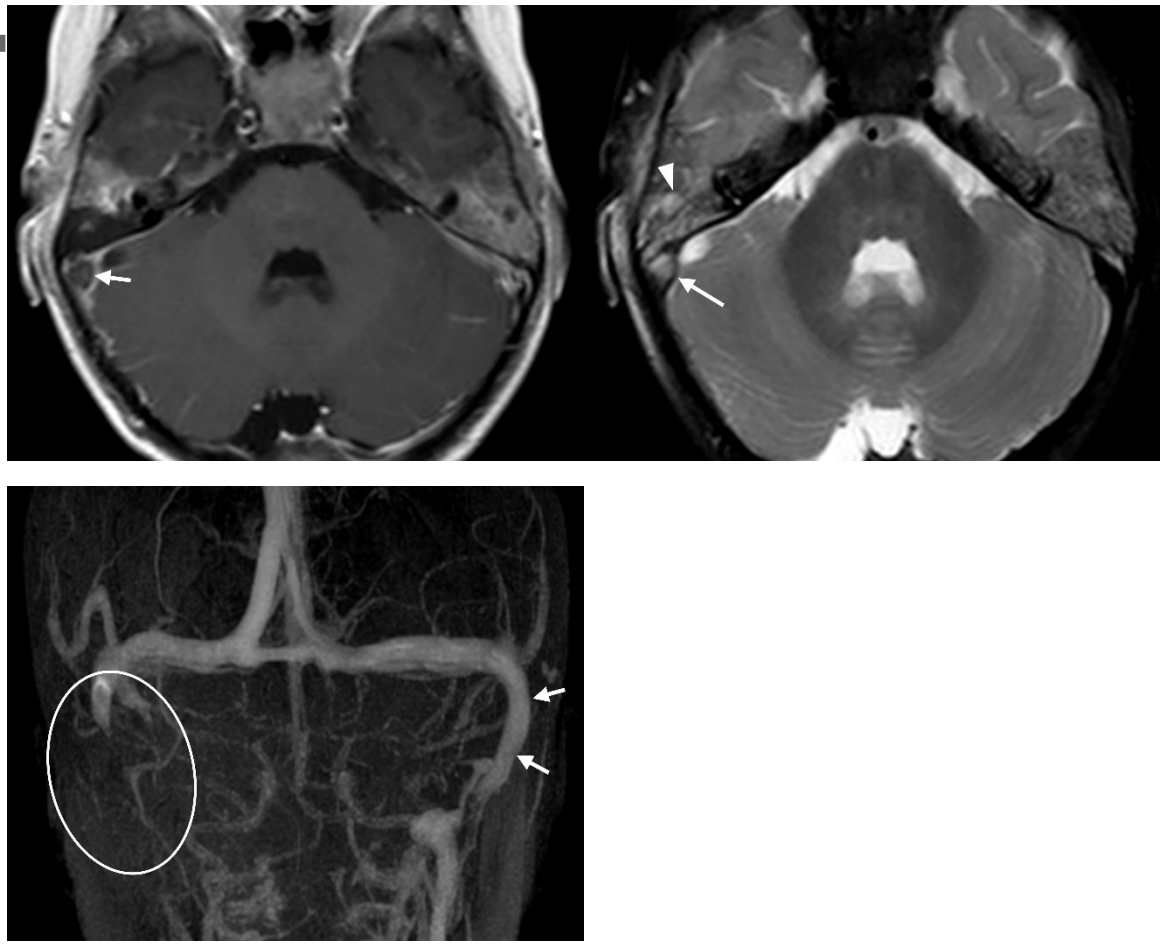

Figure 11. 3-year-old male with sigmoid sinus thrombosis associated with coalescent mastoiditis. Fat-suppressed T2-weighted image (A) shows high signal intensity in the right mastoid (arrowhead), consistent with coalescent mastoiditis, and the right sigmoid sinus with high signal intensity(arrow), indicating the loss of the flow void. Contrast enhanced T1-weighted image (B) shows enhancement defect (arrow) in the right sigmoid sinus, and MR

venography (C) shows that the right sigmoid sinus is absent (within circle) and the left sigmoid sinus (arrows).

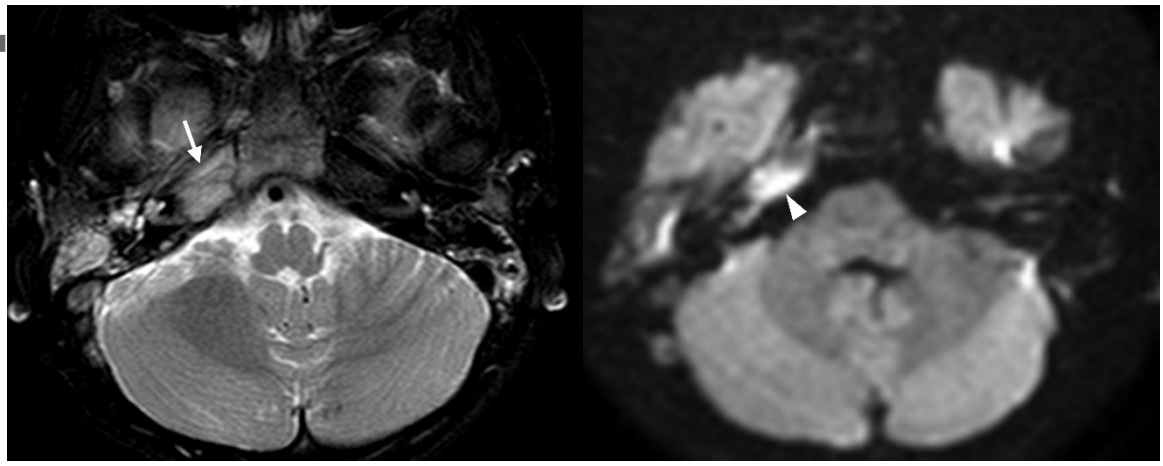

Figure 12. 6-year-old female with right petrous apicitis. Fat-suppressed T2-weighted image (A) shows high signal intensity in the right petrous apex (arrow), consistent with petrous apicitis. Diffusion-weighted imaging (B) shows localized high signal intensity in the right petrous apex (arrowhead), indicating the presence of an abscess.

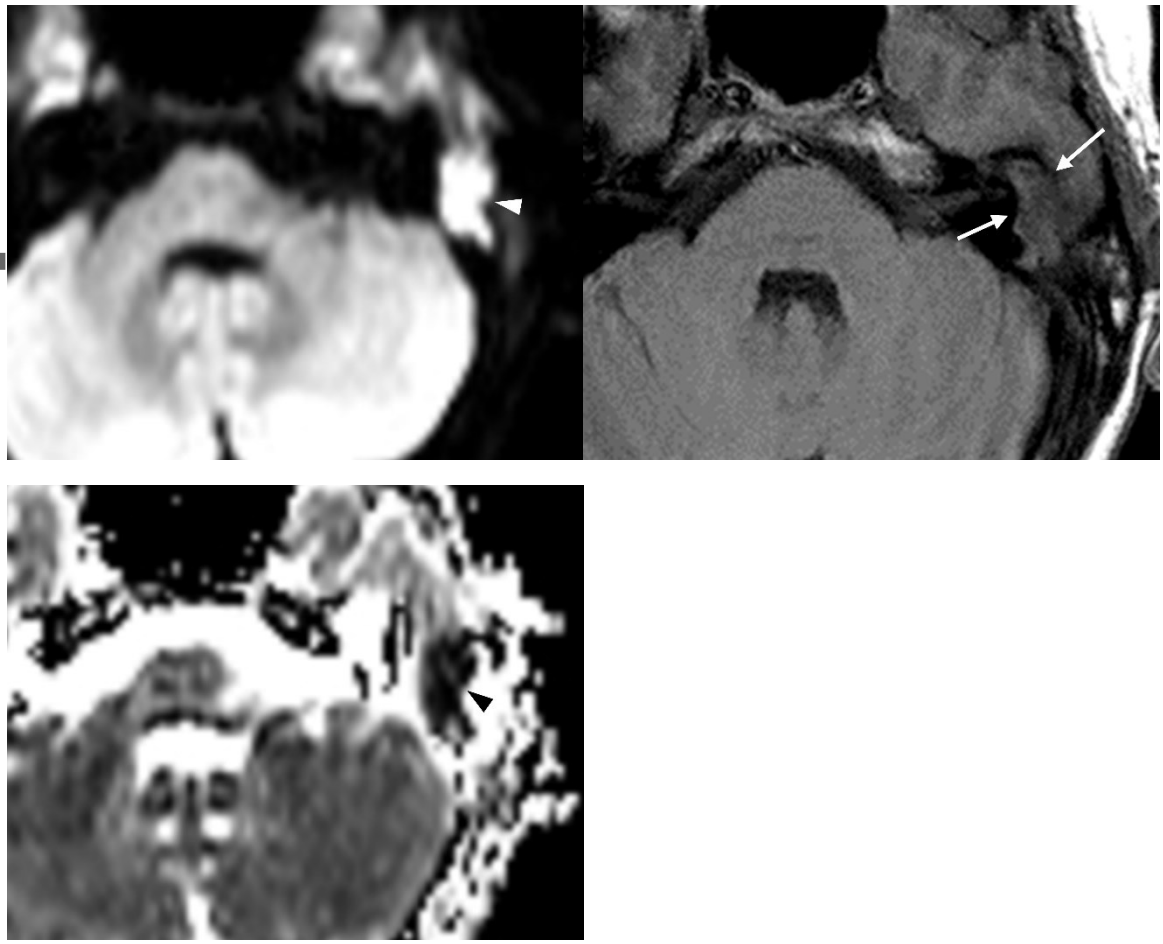

Figure 13. 12-year-old male with a cholesteatoma of the left middle ear. On preoperative evaluation, the left mastoid shows partial low signal intensity on T1-weighted image (A, arrows) and high signal intensity on diffusion-weighted imaging (B, arrowhead), indicating mastoid extension of the cholesteatoma. Surgery revealed the mastoid extension. The apparent diffusion coefficient value of the lesion is very low ($0.58 \times 10^{-3} mm^2/s$) (C, arrowhead). The disease recurred three years after surgery.

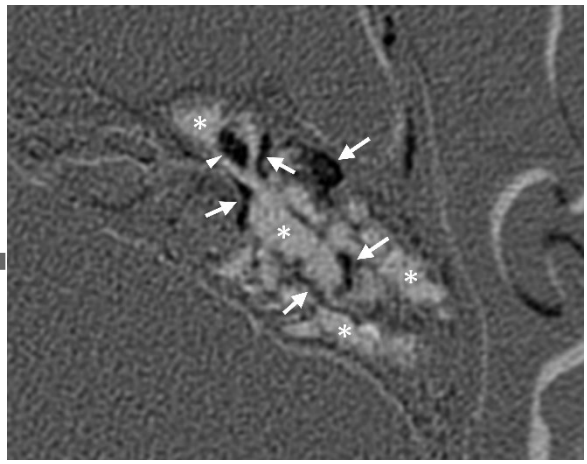

Figure 14. 46-year-old female with a cholesteatoma of the left middle ear. The temporal subtraction CT was obtained by subtracting the remote high-resolution CT (HRCT) from the preoperative HRCT. The temporal subtraction CT shows the mastoid cell wall (arrows) and ossicles (arrowhead) in black color, indicating progressive bone erosive changes. The black color in the mastoid region indicates the presence of mastoid extension of the middle ear cholesteatoma. Other areas within the tympanic cavity and mastoid are shown in white color (*), indicating increased non-specific inflammatory changes. Surgery revealed mastoid extension.

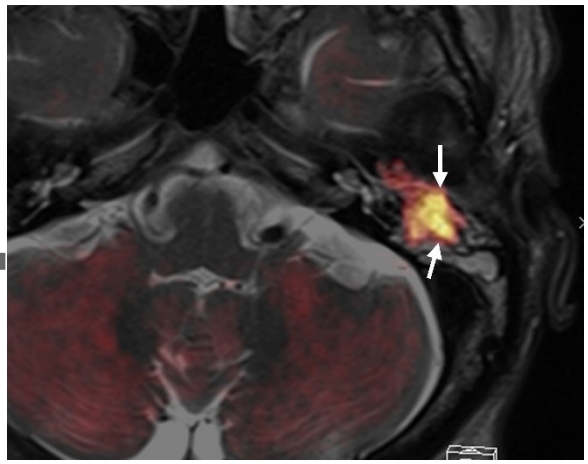

Figure 15. 42-year-old male with a cholesteatoma of the left middle ear. The fusion image of diffusion-weighted imaging and T2-weighted image clearly shows the extent of mastoid extension of the cholesteatoma, which is easy to interpret (arrows).

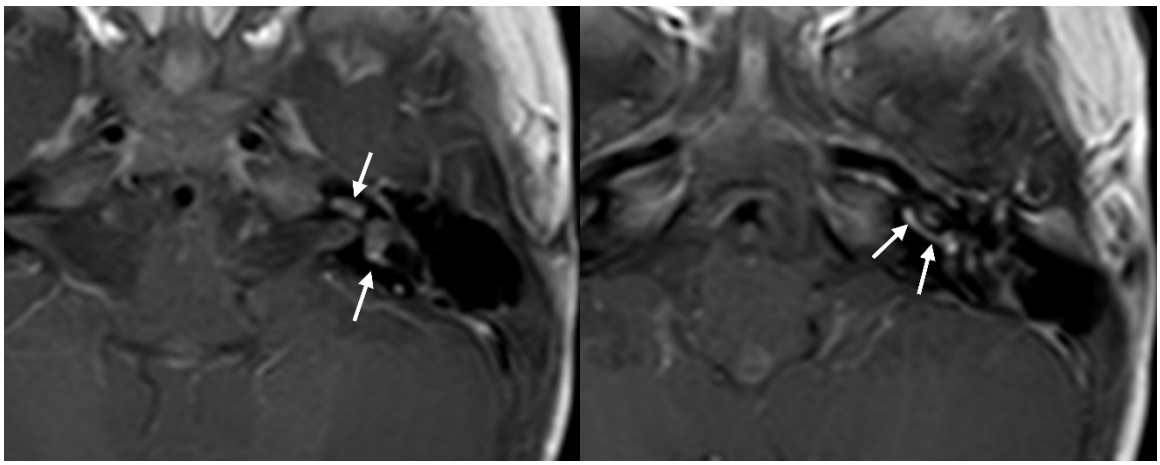

Figure 16. 12-year-old male with left labyrinthitis. Post-contrast T1-weighted image (A, B) showed enhancement (arrows) in the left inner ear, including the cochlea and vestibule, consistent with labyrinthitis.

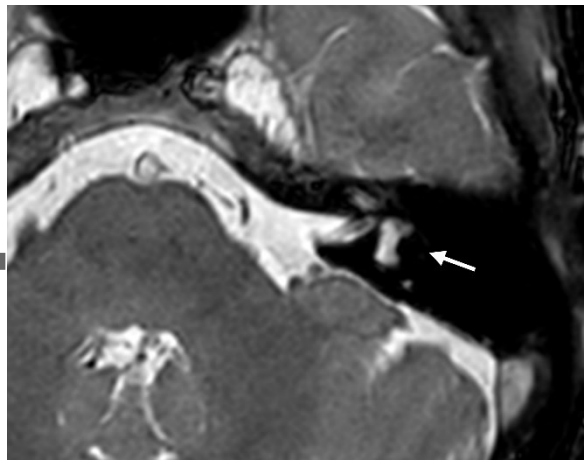

Figure 17. 67-year-old female with left labyrinthitis ossificans. 3D heavily T2-weighted image showed decreased signal intensity in the left lateral semicircular canal (arrow), consistent with left labyrinthitis ossificans.

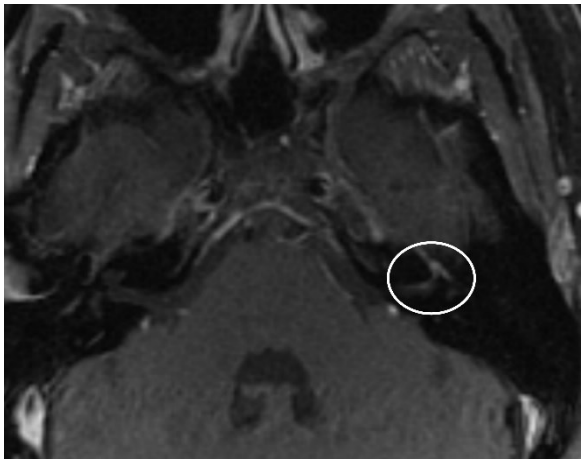

Figure 18. 45-year-old female with Bell's palsy. Contrast-enhanced fat-suppressed T1-weighted image shows an enhancement (within circle) of the facial nerve (meatal, labyrinthine, and tympanic segments).

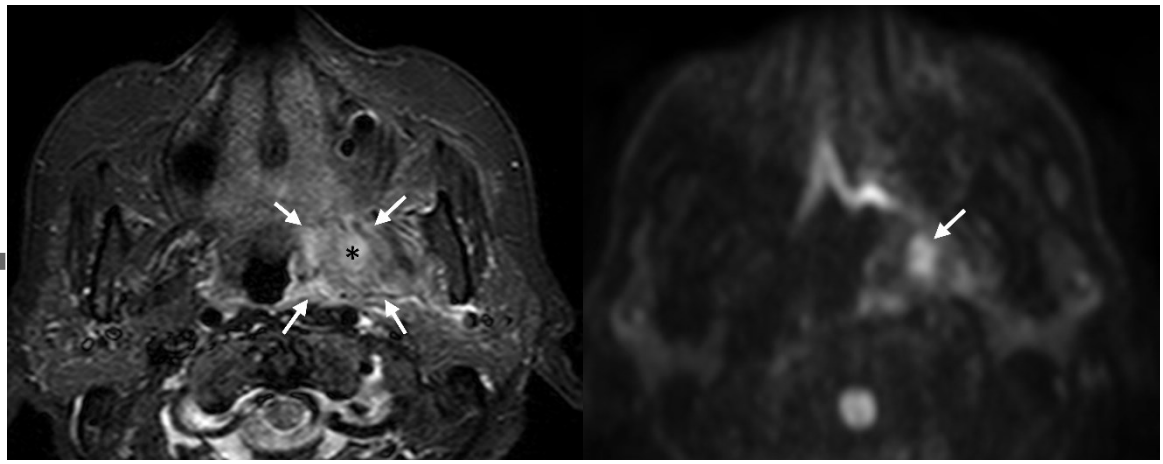

Figure 19. 65-year-old female with left peritonsillar abscess. Short tau inversion recovery (A) shows enlargement of the left palatine tonsil with peripheral edematous signal intensities (arrows) and localized high signal (*) within the lesion. Diffusion-weighted imaging (B) shows high signal intensity within the lesion (arrow), indicating a peritonsillar abscess.

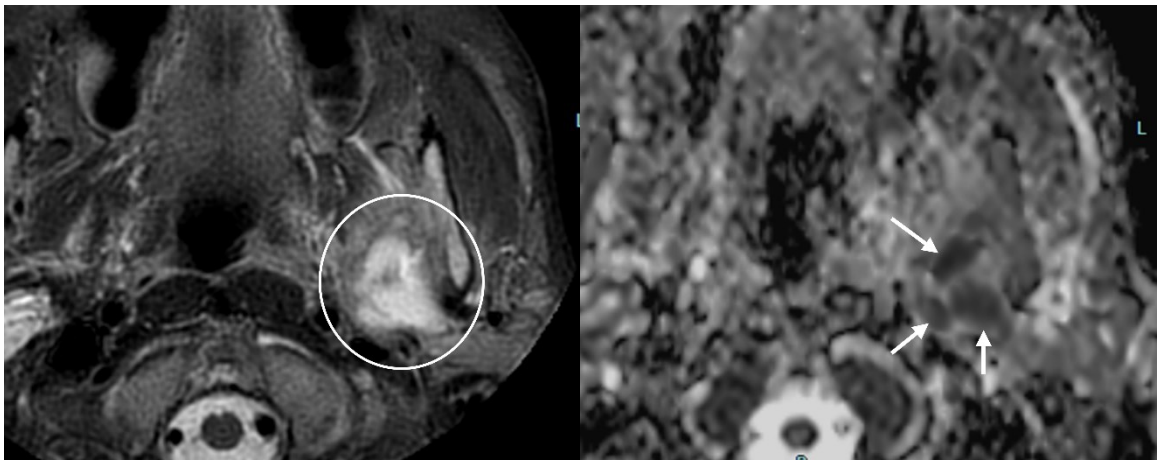

Figure 20. 57-year-old male with a masticator space abscess. Short tau inversion recovery (A) shows high signal intensities (within circle) in left masticator space with the low mean

apparent diffusion coefficient of 0.51 x 10^{-3}mm^2/s (B, arrows), indicating diffusion restriction.

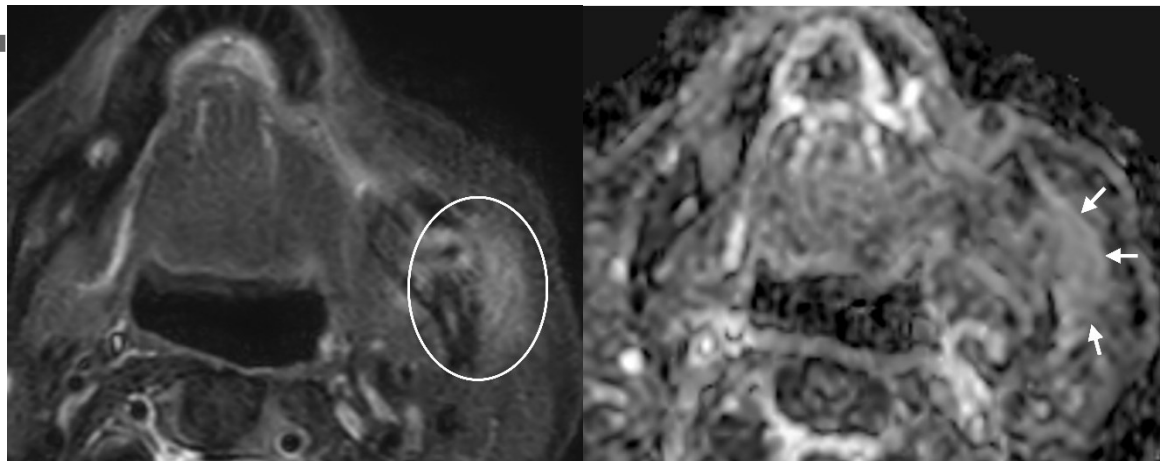

Figure 21. 77-year-old female with masticator space cellulitis. Short tau inversion recovery (A) shows high signal intensities (within circle) in left masticator space with the high mean apparent diffusion coefficient of 1.52 x 10^{-3}mm^2/s (B, arrows).

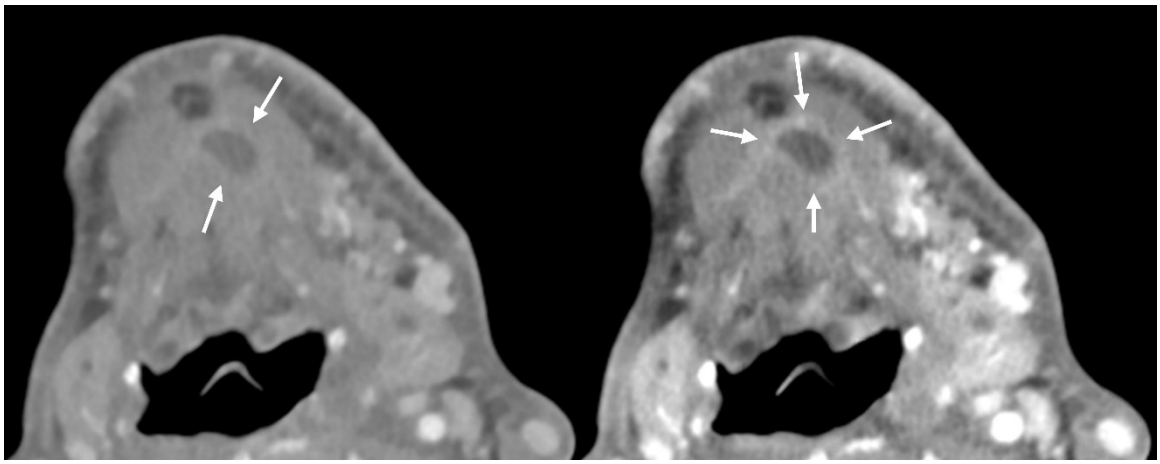

Figure 22. 76-year-old male with a sublingual abscess. The 70 keV virtual monochromatic image (A), which approximates conventional CT, shows a low density area with a rim-like

enhancement in the left sublingual space (arrows), suggestive of an abscess. The low keV (40 keV) virtual monochromatic image (B) shows the rim enhancement more clearly than the 70 keV image (arrows), which is more definitive for abscess.

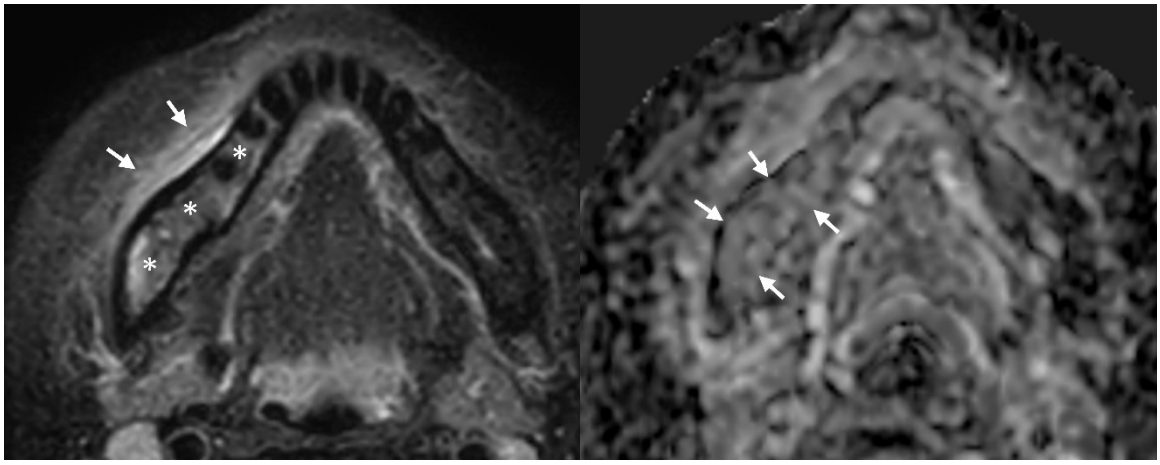

Figure 23. 46-year-old female with mandibular osteomyelitis. Short tau inversion recovery (A) shows high signal intensity (*) of the right mandible with edematous high signal intensity in the surrounding soft tissues (arrows). The mean apparent diffusion coefficient value of the lesion is elevated at 1.31 x 10^{-3} mm^2/s (B, arrows).

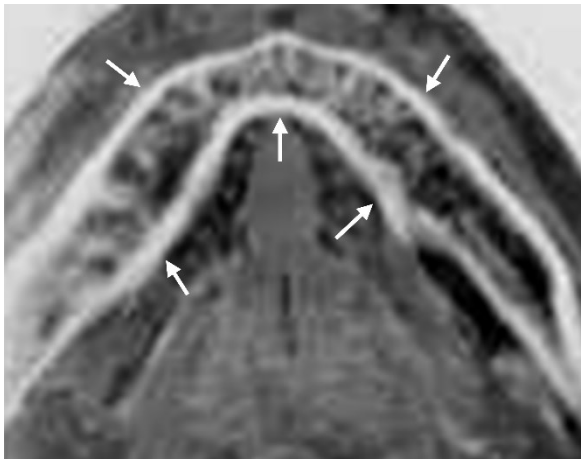

Figure 24. 48–year-old healthy male. MR bone imaging at the level of the mandible clearly shows the bony cortex and trabecula of the jaw (arrows).

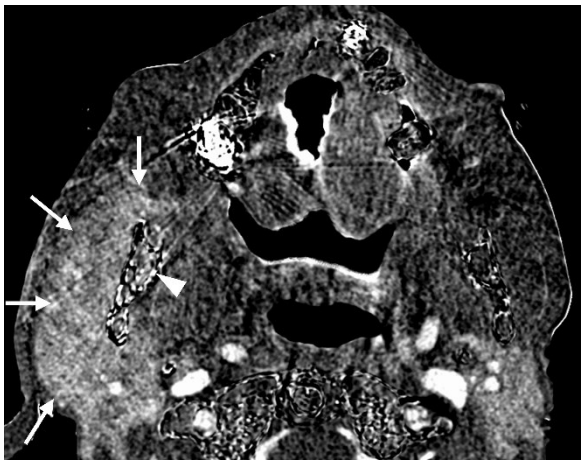

Figure 25. Female in her 90s with inflammatory spread to the masticator space from right mandibular osteomyelitis. On conventional contrast-enhanced CT (A), it is difficult to evaluate the right masticator space due to metal artifacts from dental hardware. Contrast-enhanced CT after the application of the metal artifact reduction algorithm (B) shows swelling of the right masseter muscle with mild, ill-defined enhancement (*). Subtraction iodine CT (non-enhanced CT subtracted from contrast-enhanced CT, C) shows not only

artifact reduction but also the detailed extent of inflammation (arrows), including mandibular osteomyelitis (arrowhead).

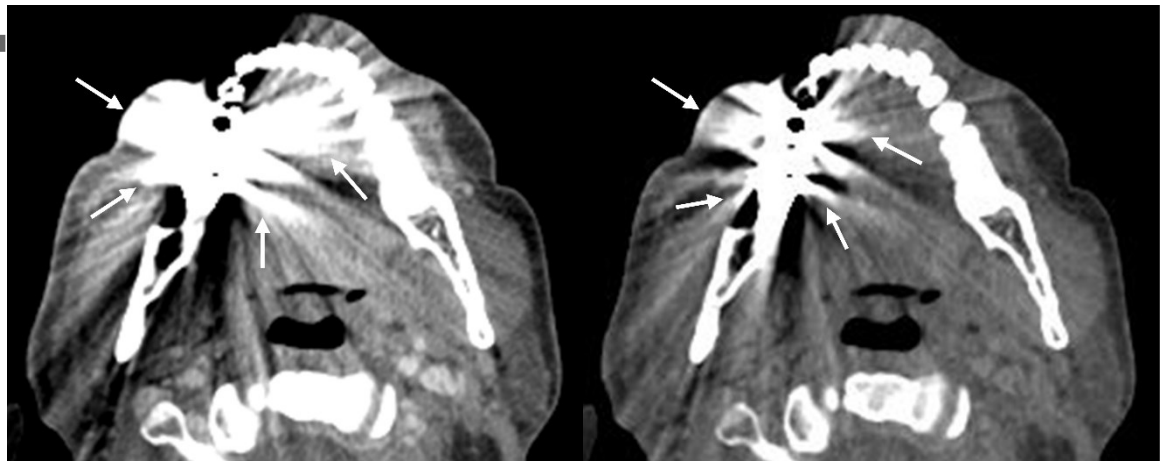

Figure 26. 52-year-old male. Compared to 70-keV virtual monochromatic imaging, which approximates conventional CT (A), 140-keV virtual monochromatic imaging (B) shows reduced dental metal artifacts (arrows).

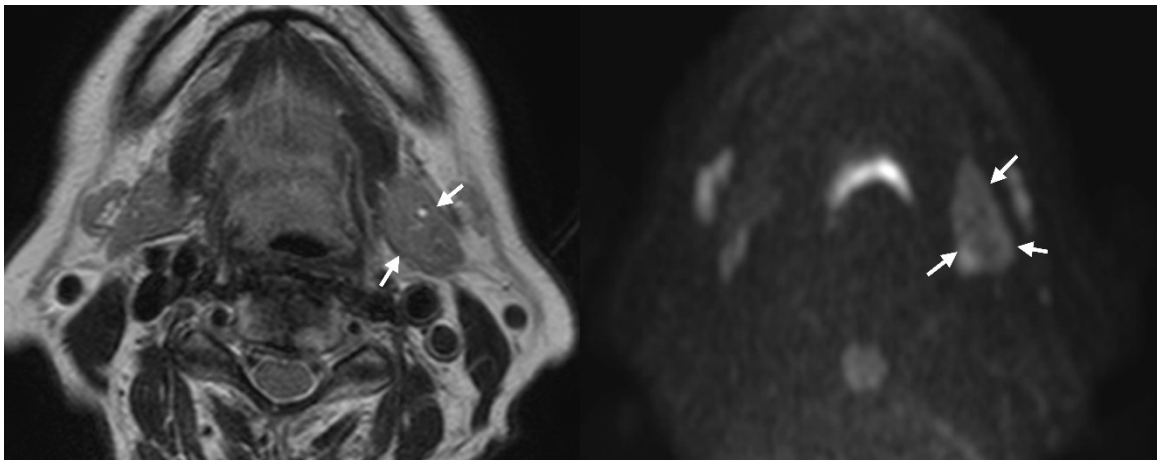

Figure 27. 72-year-old female with submandibular sialadenitis. T2-weighted image (A) shows no internal abnormal signal intensity in the slightly swollen left submandibular gland

(arrows). Diffusion-weighted imaging (B) shows a high signal intensity (arrows) in the left submandibular gland indicating submandibular adenitis.

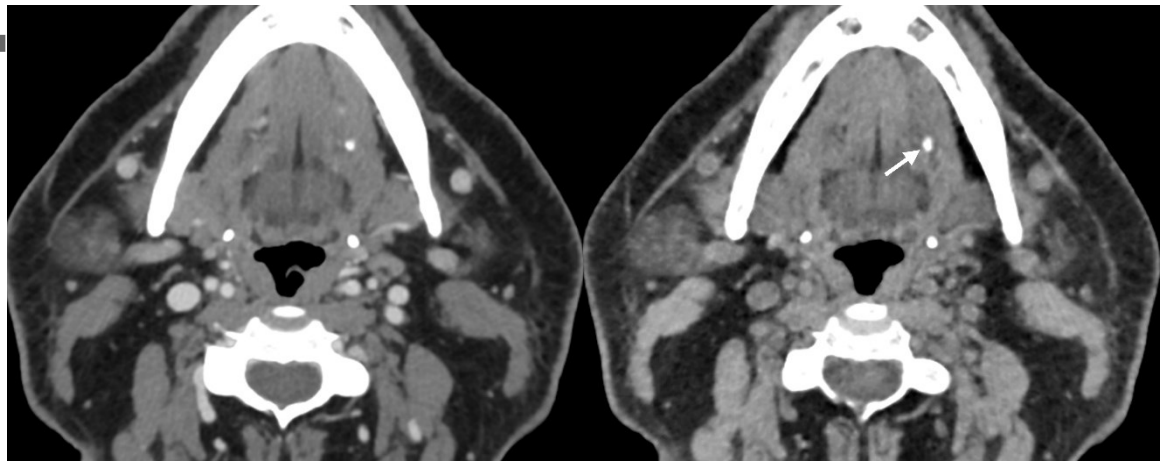

Figure 28. Virtual monochromatic imaging (B) derived from contrast-enhanced dual-energy CT (A) more easily depicts a salivary stone (arrow) of the left submandibular duct.